INTERNATIONAL JOURNAL FOR NUMERICAL METHODS IN FLUIDS
Int. J. Numer. Meth. Fluids 2009; **59**:495–518
Published online 2 June 2008 in Wiley InterScience (www.interscience.wiley.com). DOI: 10.1002/fld.1826

Numerical study of magnetohydrodynamic laminar flow separation in a channel with smooth expansion

T. K. Maikap[1], T. R. Mahapatra[2], P. Niyogi[3,*,†,‡] and A. K. Ghosh[1]

[1]*Department of Mathematics, Jadavpur University, Kolkata 700 032, India*
[2]*Department of Mathematics, Visva Bharati, Santiniketan 731235, India*
[3]*Department of Mathematics, IIT, Kharagpur, India*

SUMMARY

The flow of an electrically conducting incompressible viscous fluid in a plane channel with smooth expansion in the presence of a uniform transverse magnetic field has been analysed. A solution technique for the governing magnetohydrodynamic equations in primitive variable formulation has been developed. A co-ordinate transformation has been employed to map the infinite irregular domain into a finite regular computational domain. The governing equations are discretized using finite-difference approximations in staggered grid. Pressure Poisson equation and pressure correction formulae are derived and solved numerically. It is found that with increase in the magnetic field, the size of the flow separation zone diminishes and for sufficiently large magnetic field, the separation zone disappears completely. The peak u-velocity decreases with increase in the magnetic field. It is also found that the asymmetric flow in a symmetric geometry, which occurs at moderate Reynolds numbers, becomes symmetric with sufficient increase in the transverse magnetic field. Thus, a transverse magnetic field of suitable strength has a stabilizing effect in controlling flow separation, as also in delaying the transition to turbulence. Copyright © 2008 John Wiley & Sons, Ltd.

Received 1 June 2006; Revised 18 March 2008; Accepted 24 March 2008

KEY WORDS: viscous flow; laminar flow; channel flow; channel with symmetric expansion; transverse magnetic field in flow separation; Hartmann flow; separation control

1. INTRODUCTION

The study of laminar flow in tubes or channels with constriction or expansion has received considerable attention in recent years, in view of engineering applications. Lee and Fung [1] obtained numerical solution for flow in a tube with constriction at low Reynolds number. Lee [2]

*Correspondence to: P. Niyogi, 42A Naskarpara Road, Santoshpur, Kolkata 700 075, India.
†E-mail: pradipni@cal2.vsnl.net.in
‡Retired.

investigated steady laminar flow through a variable constriction in a vascular tube. Cheng [3] investigated steady viscous flow through a channel with symmetric cosinusoidal constrictions on both the walls at the same location. Vradis *et al.* [4] studied steady incompressible viscous flow in a channel with local constriction having the shape of a Gaussian distribution. Mahapatra *et al.* [5] studied flow separation in a constricted channel without assuming flow symmetry about the channel centreline. They observed that with increasing Reynolds number, the flow through a channel with smooth symmetric constriction may become asymmetric about the channel centreline.

For the case of symmetric sudden channel expansion, at low Reynolds numbers, there is no separation and the flow is symmetric. As the Reynolds number increases, the flow separates from the walls with the formation of recirculation zones of unequal length and the flow becomes asymmetric. With further increase in Reynolds number, the asymmetric flow separates from one of the walls and gets attached to the other. This was found by several authors like Durst *et al.* [6, 7], Cherdron *et al.* [8], and by Fearn *et al.* [9]. As the Reynolds number increases, the asymmetry remains in the flow, even up to turbulent flow conditions as observed by Restivo and Whitelaw [10]. This phenomenon is referred to in the literature as the 'Coanda effect'. Instabilities and bifurcations of channel flows have been investigated by Sobey and Drazin [11].

Recently, Pramanik *et al.* [12] numerically studied viscous flow through a symmetrically expanded channel. They found that in the case of smooth local expansion, the flow becomes asymmetric about the channel centreline with increasing Reynolds number.

The control of boundary layer separation is of much practical interest in aerodynamics and in physiological flows. Several methods have been developed for the purpose of artificially controlling the behaviour of the boundary layer. The aim of these methods is to alter and organize the whole flow in a desired direction by influencing the structure of the boundary layer [13]. Fluid flow separation and various boundary layer control techniques were described in Gad-el-Hak and Bushnell [14]. The application of magnetohydrodynamic (MHD) principles is yet another method for affecting the flow field in a desired direction by altering the structure of the boundary layer. Recently, Midya *et al.* [15] investigated MHD viscous flow in a channel with constriction. They found that the flow separates downstream of the peak of the constriction and that, with increase in magnetic field the flow separation zone diminishes in size. For sufficiently large magnetic field, the separation zone disappears completely.

Recently, stability and transition to turbulence in plane channel flow have been investigated in several works. Stability thresholds of streamwise streaks and transition to turbulence in plane channel flow were investigated by Reddy *et al.* [16]. Direct numerical simulation was applied by Krasnov *et al.* [17] to investigate instability and transition to turbulence of flow of an electrically conducting incompressible fluid between two parallel unbounded insulating walls affected by a wall-normal magnetic field (the Hartmann flow). The transition to turbulence that arise in MHD flows in ducts was investigated experimentally by Moresco and Alboussiere [18].

In this paper viscous flow of an electrically conducting incompressible fluid in a channel with a symmetric smooth expansion is studied numerically without assuming flow symmetry with respect to the channel centreline. The flow is permeated by uniform magnetic field applied normal to the plane of the channel wall. A co-ordinate transformation has been used to map an infinite irregular domain into a finite rectangular computational domain. The governing equations have been discretized on a staggered grid using a finite-difference method, popularly known as MAC method [19, 20]. It is found that flow separation may be controlled by applying a transverse magnetic field of suitable strength.

DOI: 10.1002/fld

2. GOVERNING EQUATIONS

We consider the two-dimensional flow of a homogeneous Newtonian incompressible viscous electrically conducting fluid in an infinitely long parallel plate channel, having symmetric smooth expansions on both the plates at the same location (as shown in Figure 1). Let σ be the electrical conductivity and ρ the density of the fluid. Initially, the fluid is at rest everywhere within the channel except at an infinite distance upstream of the expansion where a Hartmann profile is prescribed.

Let (x^*, y^*, z^*) be the Cartesian co-ordinates of any point in the flow domain, where the x^*-axis is along the bottom plate and the y^*-axis is normal to both the plates. Let u^*,v^* be the velocity components along the x^* and y^* directions, respectively, p^* the pressure, $U/4$ be the centreline velocity for a parallel flow in the channel far upstream of the expansion, and v the kinematic viscosity. A uniform magnetic field B_0 is imposed along y^* axis (as shown in Figure 1).

The governing continuity equation can be expressed as

$$\frac{\partial u^*}{\partial x^*}+\frac{\partial v^*}{\partial y^*}=0 \tag{1}$$

Taking into account the Lorentz forces due to MHD interactions, the simplified momentum equations in the x^* and y^* directions may be expressed as

$$\frac{\partial u^*}{\partial t^*}+u^*\frac{\partial u^*}{\partial x^*}+v^*\frac{\partial u^*}{\partial y^*}=-\frac{1}{\rho}\frac{\partial p^*}{\partial x^*}+\nu\left(\frac{\partial^2 u^*}{\partial x^{*2}}+\frac{\partial^2 u^*}{\partial y^{*2}}\right)-\frac{\sigma B_0^2}{\rho}u^* \tag{2}$$

and

$$\frac{\partial v^*}{\partial t^*}+u^*\frac{\partial v^*}{\partial x^*}+v^*\frac{\partial v^*}{\partial y^*}=-\frac{1}{\rho}\frac{\partial p^*}{\partial y^*}+\nu\left(\frac{\partial^2 v^*}{\partial x^{*2}}+\frac{\partial^2 v^*}{\partial y^{*2}}\right) \tag{3}$$

respectively, where the induced magnetic field is assumed to be negligible in comparison with the external magnetic field, which is justified for MHD flow at small magnetic Reynolds numbers [21]. In fact, such an assumption is valid for flow of liquid metals (e.g. mercury or liquid sodium).

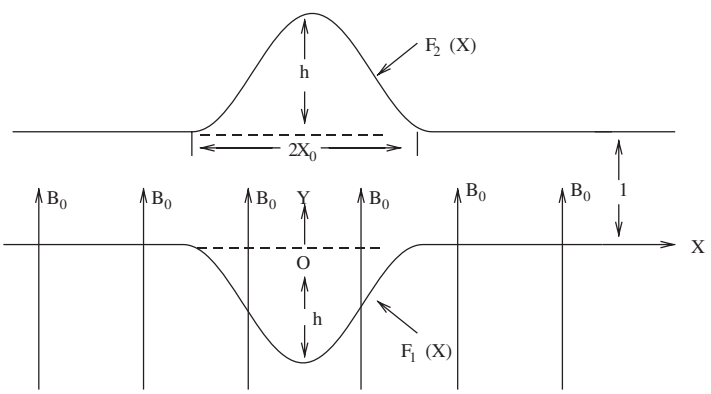

Figure 1. A sketch of the physical problem.

DOI: 10.1002/fld

Further, electrical conductivity σ of the fluid is assumed constant. (For mercury, $\sigma=10^{-5}$ e.m.u and for liquid sodium, $\sigma=10^{-4}$ e.m.u.) It is also assumed that the external electric field is zero and the electrical field due to polarization of charges is negligible.

Introducing the following non-dimensional variables:

$$t=\frac{t^*U}{h^*},\quad X=\frac{x^*}{h^*},\quad Y=\frac{y^*}{h^*},\quad u=\frac{u^*}{U},\quad v=\frac{v^*}{U},\quad p=\frac{p^*}{\rho U^2} \tag{4}$$

the above magnetohydrodynamical equations for incompressible viscous electrically conducting fluid flow in non-dimensional form become

$$\frac{\partial u}{\partial X}+\frac{\partial v}{\partial Y}=0 \tag{5}$$

$$\frac{\partial u}{\partial t}+\frac{\partial u^2}{\partial X}+\frac{\partial uv}{\partial Y}=-\frac{\partial p}{\partial X}+\frac{1}{Re}\left(\frac{\partial^2 u}{\partial X^2}+\frac{\partial^2 u}{\partial Y^2}\right)-\frac{1}{Re}M^2u \tag{6}$$

$$\frac{\partial v}{\partial t}+\frac{\partial uv}{\partial X}+\frac{\partial v^2}{\partial Y}=-\frac{\partial p}{\partial Y}+\frac{1}{Re}\left(\frac{\partial^2 v}{\partial X^2}+\frac{\partial^2 v}{\partial Y^2}\right) \tag{7}$$

where $Re(=Uh^*/v)$ is the Reynolds number, $M(=B_0h^*\sqrt{\sigma/\rho v})$ is the Hartmann number, and h^* is the width of the straight part of the channel. The parameter M^2/Re is normally called *magnetic interaction parameter or Stuart number.* It may be noted that the above equations are expressed in a conservative form using the continuity equation.

2.1. Boundary conditions

The streamwise and transverse velocity components should be zero at the rigid walls (no-slip condition). At the inlet and outlet boundaries, the Hartmann velocity profile [21] is prescribed. On the upper ($Y=F_2(X)$) and lower ($Y=F_1(X)$) walls of the channel, the no-slip boundary conditions are

$$u=0,\quad v=0\quad \text{at } Y=F_2(X), F_1(X) \tag{8}$$

The functions $F_1(X)$ and $F_2(X)$, which represent the shapes of the lower and upper walls of the channel (as shown in Figure 1), are given by

$$\begin{aligned} F_1(X)&=\begin{cases} -\dfrac{1}{2}h\left(1+\cos\left(\dfrac{\pi X}{X_0}\right)\right):|X|\leqslant X_0\\ 0:|X|\geqslant X_0 \end{cases}\\ F_2(X)&=\begin{cases} 1+\dfrac{1}{2}h\left(1+\cos\left(\dfrac{\pi X}{X_0}\right)\right):|X|\leqslant X_0\\ 1:|X|\geqslant X_0 \end{cases} \end{aligned} \tag{9}$$

Here h is an expansion parameter. The inlet flow upstream and the outlet flow far downstream of the expansion are assumed to be the Poiseuille flow in the absence of a magnetic field and

DOI: 10.1002/fld

the Hartmann flow, [22], in the presence of magnetic field. In particular, we have the following conditions at inlet ($X=-\infty$) and at the outlet ($X=+\infty$) boundaries, as shown in details in [15],

$$\begin{aligned} u &= Y-Y^2 \quad \text{for } M=0 \\ u &= \frac{\cosh(M/2)-\cosh(M(Y-\frac{1}{2}))}{8\sinh^2(M/4)} \quad \text{for } M\neq 0 \end{aligned} \tag{10}$$

2.2. Initial condition

The initial condition is that there is no flow inside the flow domain, while on the other hand, the parabolic velocity profile is prescribed at the inlet boundary in the case of $M=0$ and the Hartmann profile is prescribed at the inlet boundary in the case of $M\neq 0$. Physically, this implies the flow is approaching the expansion gradually.

3. CO-ORDINATE TRANSFORMATION

Application of the boundary conditions at the various boundaries is a difficult task. It is somewhat unsatisfactory to simply impose the far-field boundary conditions at large finite distances, since, for flows with increasing Reynolds number, the disturbances created by the irregular shape are sizable even at far downstream. The flow is expected to become smoother far away from the expansion and the grid should necessarily be more refined near the expansion than that far away from it. Again, the prescription of conditions at boundaries not conforming to the co-ordinate lines leads to severe interpolation errors. For these reasons, a transformation is introduced to map the infinite irregular physical domain to a finite rectangular computational domain. The co-ordinate transformation used in this study is

$$x=\tanh(kX), \quad y=\frac{Y-F_1(X)}{F_2(X)-F_1(X)} \tag{11}$$

where k is a parameter that controls the grid distribution in an efficient manner. The grids in the physical plane are dense near the origin due to the nature of the function $\tanh(kX)$. The transformation defined in (11) transforms the curved upper boundary $Y=F_2(X)$ into the straight line $y=1$, the curved lower boundary $Y=F_1(X)$ into the straight line $y=0$ and the outflow and inflow boundaries at $X=\pm\infty$ into $x=\pm 1$.

Using the chain rule of differentiation, the continuity equation (5) changes to

$$k(1-x^2)\frac{\partial u}{\partial x}-k(1-x^2)G(x,y)\frac{\partial u}{\partial y}+\frac{1}{f_2(x)-f_1(x)}\frac{\partial v}{\partial y}=0 \tag{12}$$

and the momentum equations ((6) and (7)) transform to

$$\begin{aligned} &\frac{\partial u}{\partial t}+k(1-x^2)\frac{\partial u^2}{\partial x}-k(1-x^2)G(x,y)\frac{\partial u^2}{\partial y}+\frac{1}{f_2(x)-f_1(x)}\frac{\partial uv}{\partial y} \\ &\quad =-k(1-x^2)\frac{\partial p}{\partial x}+k(1-x^2)G(x,y)\frac{\partial p}{\partial y}+\frac{1}{Re}\left[k^2(1-x^2)^2\frac{\partial^2 u}{\partial x^2}\right. \end{aligned}$$

DOI: 10.1002/fld

$$-2k^2x(1-x^2)\frac{\partial u}{\partial x}-\{k^2(1-x^2)^2\{H(x,y)-2G(x,y)L(x)\}$$

$$-2k^2x(1-x^2)G(x,y)\}\frac{\partial u}{\partial y}-2k^2(1-x^2)^2G(x,y)\frac{\partial^2 u}{\partial x\partial y}+\left\{k^2(1-x^2)^2G^2(x,y)\right.$$

$$\left.+\frac{1}{\{f_2(x)-f_1(x)\}^2}\right\}\frac{\partial^2 u}{\partial y^2}\Bigg]-\frac{M^2}{Re}u \tag{13}$$

$$\frac{\partial v}{\partial t}+k(1-x^2)\frac{\partial uv}{\partial x}-k(1-x^2)G(x,y)\frac{\partial uv}{\partial y}+\frac{1}{f_2(x)-f_1(x)}\frac{\partial v^2}{\partial y}$$

$$=-\frac{1}{f_2(x)-f_1(x)}\frac{\partial p}{\partial y}+\frac{1}{Re}\left[k^2(1-x^2)^2\frac{\partial^2 v}{\partial x^2}-2k^2x(1-x^2)\frac{\partial v}{\partial x}\right.$$

$$-\{k^2(1-x^2)^2\{H(x,y)-2G(x,y)L(x)\}-2k^2x(1-x^2)G(x,y)\}\frac{\partial v}{\partial y}$$

$$\left.-2k^2(1-x^2)^2G(x,y)\frac{\partial^2 v}{\partial x\partial y}+\left\{k^2(1-x^2)^2G^2(x,y)+\frac{1}{\{f_2(x)-f_1(x)\}^2}\right\}\frac{\partial^2 v}{\partial y^2}\right] \tag{14}$$

where

$$\begin{aligned}
&F_i(X)=f_i(x), \quad F_i'(X)=k(1-x^2)f_i'(x)\\
&F_i''(X)=k(1-x^2)[-2kxf_i'(x)+k(1-x^2)f_i''(x)], \quad i=1,2\\
&G(x,y)=\frac{yf_2'(x)+(1-y)f_1'(x)}{f_2(x)-f_1(x)}, \quad H(x,y)=\frac{yf_2''(x)+(1-y)f_1''(x)}{f_2(x)-f_1(x)}\\
&L(x)=\frac{f_2'(x)-f_1'(x)}{f_2(x)-f_1(x)}, \quad X=\frac{1}{2k}\ln\left(\frac{1+x}{1-x}\right), \quad -1\leqslant x\leqslant 1
\end{aligned} \tag{15}$$

and the prime denotes derivative with respect to the argument.

The boundary conditions in the transformed co-ordinate system are

$$u=0, \quad v=0 \quad \text{at } y=0,1 \tag{16}$$

The inlet velocity profile at $x=-1$ and the outlet velocity profile at $x=+1$ are both given by

$$\begin{aligned}
&u=y-y^2 \quad \text{for } M=0\\
&u=\frac{\cosh(M/2)-\cosh(M(y-\frac{1}{2}))}{8\sinh^2(M/4)} \quad \text{for } M\neq 0
\end{aligned} \tag{17}$$

DOI: 10.1002/fld

4. NUMERICAL SOLUTION

Solution of the governing equations under appropriate initial and boundary conditions offers the prospect of predicting laminar separated flow which, in view of their complex structure, is beyond the scope of analytical treatment. We solve them numerically in the computational plane employing a finite-difference technique on staggered grid. To express the derivatives in the transformed governing equations in terms of finite-difference formula, a suitable grid arrangement is needed.

4.1. Type of grid used

Typical grid distributions in the physical plane for the symmetric expansion are shown in Figure 2. In this plane, grids are non-uniformly spaced. The transformation defined in Section 3 enables one to space grid points uniformly in the computational plane. In the new system of co-ordinates (x, y), a uniformly spaced rectangular grid is superimposed on $[-1, 1] \times [0, 1]$ computational domain. All the computations have been carried out in this rectangular domain. In the present method one type of staggered grid, popularly known as MAC cell [19], is used. In this type of grid arrangement, the velocities and the pressure are evaluated at different cell positions as shown in Figure 3: u-velocity at the middle of the vertical sides of the cell, v-velocity at the middle of the horizontal sides, and pressure at the cell centre.

4.2. Finite-difference representation

It may be noted that the continuity equation for an incompressible flow contains only the velocity components and no direct link with the pressure is available. The primitive variables (u, v, p) for two-dimensional flow in non-staggered conventional grids get coupled to every alternate node if centred differences are used for representing the derivatives, giving rise to 'checker-board effect' [20]. On the other hand, the use of staggered grid permits coupling of the u, v and p solutions at adjacent grid points, thus preventing the appearance of oscillatory solutions, particularly for the pressure p.

The finite-difference equations are derived in three distinct types of cells viz., (i) continuity cell, (ii) u-momentum cell, and (iii) v-momentum cell [23], respectively, for the three governing equations. The time derivative terms in all the equations are differenced according to the first-order accurate, two-level, forward-time differencing formula. The convective terms in the momentum equations are differenced with a hybrid formula consisting of central differencing and second-order

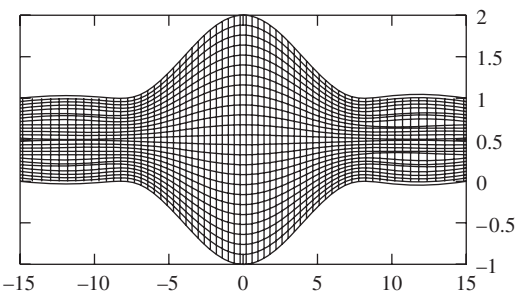

Figure 2. A typical grid alignment in the physical plane for the symmetric expansion.

DOI: 10.1002/fld

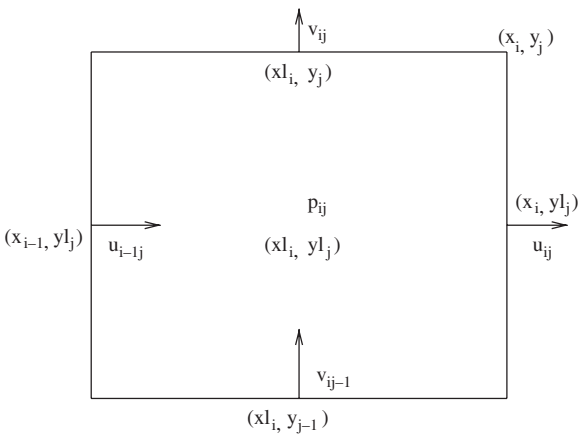

Figure 3. Arrangement of dependent variables in a typical MAC cell.

upwinding [24]. The diffusive terms are differenced using a second-order accurate, three-point, central-difference formula. The source terms are centrally differenced keeping the position of the respective fluxes at the centres of the control volumes.

With $t=n\delta t,\ x=i\delta x,\ y=j\delta y$ the difference forms of p, u, v are expressed as

$$p(x,y,t)=p_{ij}^n,\quad u(x,y,t)=u_{ij}^n \quad \text{and} \quad v(x,y,t)=v_{ij}^n$$

where superscript n refers to the time direction, subscripts i and j refer to the spatial directions, δt is the time increment and $\delta x, \delta y$ are the length and width of the control volumes. Discretization of the continuity equation (12) at the (i, j)th cell takes the form

$$k(1-xl_i^2)\frac{u_{ij}^n-u_{i-1j}^n}{\delta x}-k(1-xl_i^2)G(xl_i,yl_j)\frac{u_{\mathrm{tc}}-u_{\mathrm{bc}}}{\delta y}+\frac{1}{f_2(xl_i)-f_1(xl_i)}\frac{v_{ij}^n-v_{ij-1}^n}{\delta y}=0 \tag{18}$$

where the quantities xl_i, yl_j, u_{tc} and u_{bc} are defined as

$$\begin{aligned} xl_i &= x_i-\frac{\delta x}{2},\quad yl_j=y_j-\frac{\delta y}{2}\\ u_{\mathrm{tc}} &= 0.25(u_{ij}^n+u_{i-1j}^n+u_{i-1j+1}^n+u_{ij+1}^n)\\ u_{\mathrm{bc}} &= 0.25(u_{ij-1}^n+u_{i-1j-1}^n+u_{i-1j}^n+u_{ij}^n) \end{aligned} \tag{19}$$

Here (xl_i, yl_j) and (x_i, y_j) are the co-ordinates of the cell centre and right top-corner of the cell, respectively, subscripts tc and bc correspond to top and bottom middle positions of the continuity cell, respectively. Thus, u_{tc} and u_{bc} stand for u-velocities at the top and bottom middle positions of the continuity cell, respectively. Considering the source, convective and diffusive terms at the nth time level, the momentum equation in the x-direction, Equation (13) may be rewritten in finite-difference form as

$$\frac{u_{ij}^{n+1}-u_{ij}^n}{\delta t}=k(1-x_i^2)\frac{p_{ij}^n-p_{i+1j}^n}{\delta x}+k(1-x_i^2)G(x_i,yl_j)\frac{p_{\mathrm{t}}-p_{\mathrm{b}}}{\delta y}+\mathrm{Ucd}_{ij}^n \tag{20}$$

DOI: 10.1002/fld

where p_t, p_b, and Ucd_{ij}^n are defined as follows:

$$p_t = 0.25(p_{ij}^n + p_{i+1j}^n + p_{ij+1}^n + p_{i+1j+1}^n) \tag{21}$$

$$p_b = 0.25(p_{ij}^n + p_{i+1j}^n + p_{ij-1}^n + p_{i+1j-1}^n) \tag{22}$$

$$\mathrm{Ucd}_{ij}^n = \frac{1}{Re}\mathrm{Diff}\,u_{ij}^n - \mathrm{Con}\,u_{ij}^n - \frac{M^2}{Re}u_{ij}^n \tag{23}$$

Here $\mathrm{Diff}\,u_{ij}^n$ and $\mathrm{Con}\,u_{ij}^n$ are the diffusive and convective terms of the u-momentum equation at the nth time level at (i, j)th cell. Subscripts t and b correspond to top and bottom middle positions of the u-momentum cell, respectively. Therefore, p_t and p_b stand for pressure at top and bottom middle positions of the u-momentum cell, respectively. The diffusive terms are discretized centrally as

$$\frac{\partial^2 u}{\partial x^2} = \frac{u_{i+1j}^n - 2u_{ij}^n + u_{i-1j}^n}{(\delta x)^2} + O(\delta x^2) \tag{24}$$

$$\frac{\partial^2 u}{\partial y^2} = \frac{u_{ij+1}^n - 2u_{ij}^n + u_{ij-1}^n}{(\delta y)^2} + O(\delta y^2) \tag{25}$$

A central-difference formula is used for the mixed derivative $\partial^2 u/\partial x \partial y$ in uniform grid.

In the present scheme, as mentioned earlier, the convective terms are differenced with a combination of central differencing and second-order upwind differencing schemes, as explained in detail in [20, 25].

Thus, finite-difference form of the u-momentum equation is given by

$$\frac{\partial u^2}{\partial x} = (1-\beta)\frac{u_r^2 - u_l^2}{\delta x} + \beta\frac{u_r\phi_{ur} - u_l\phi_{ul}}{\delta x} \tag{26}$$

$$\frac{\partial u^2}{\partial y} = (1-\beta)\frac{u_t^2 - u_b^2}{\delta y} + \beta\frac{u_t\phi_{ut} - u_b\phi_{ub}}{\delta y} \tag{27}$$

$$\frac{\partial uv}{\partial y} = (1-\beta)\frac{u_t v_t - u_b v_b}{\delta y} + \beta\frac{v_t\phi_{ut} - v_b\phi_{ub}}{\delta y} \tag{28}$$

where β is a combination factor that is determined from the stability (see Section 4.5). With $\beta = 0$ the scheme becomes central differencing and with $\beta = 1$ it is a second-order upwind difference scheme.

Similarly, the finite-difference representation for the momentum equation in the y-direction, Equation (14) is

$$\frac{v_{ij}^{n+1} - v_{ij}^n}{\delta t} = \frac{1}{f_2(xl_i) - f_1(xl_i)}\left(\frac{p_{ij}^n - p_{ij+1}^n}{\delta y}\right) + \mathrm{Vcd}_{ij}^n \tag{29}$$

where

$$\mathrm{Vcd}_{ij}^n = \frac{1}{Re}\mathrm{Diff}\,v_{ij}^n - \mathrm{Con}\,v_{ij}^n \tag{30}$$

DOI: 10.1002/fld

Here, $\mathrm{Diff}\, v_{ij}^n$ and $\mathrm{Con}\, v_{ij}^n$ are the finite-difference representation of the diffusive and convective terms of the v-momentum equation at the nth time level at the cell (i, j). The diffusive and convective terms in the v-momentum equation are differenced similarly. For representing the v-momentum convective fluxes, the same criteria have been employed as those in the u-momentum equation.

4.3. The Poisson equation for pressure

The Poisson equation for pressure is derived by combining the discretized form of the momentum and continuity equations [20]. Proceeding as in Maikap *et al.* [25], the final form of the Poisson equation for pressure is as follows:

$$\begin{aligned}&(A+B+C+D)p_{ij}^n - Ap_{i+1j}^n - Bp_{i-1j}^n + (F-E-D)p_{ij-1}^n + (E-F-C)p_{ij+1}^n \\ &\quad + E(p_{i+1j+1}^n - p_{i+1j-1}^n) + F(p_{i-1j-1}^n - p_{i-1j+1}^n) \\ &= -\left[\frac{\mathrm{Div}_{ij}^n}{\delta t} + k(1-xl_i^2)\frac{\mathrm{Ucd}_{ij}^n - \mathrm{Ucd}_{i-1j}^n}{\delta x} + \frac{\mathrm{Vcd}_{ij}^n - \mathrm{Vcd}_{ij-1}^n}{(f_2(xl_i) - f_1(xl_i))\delta y}\right]\end{aligned} \tag{31}$$

Here Div_{ij}^n is the finite-difference representation of the divergence of velocity field at cell (i, j). The detailed derivation of the Poisson equation for pressure is omitted here. The expressions for A, B, C, D, E, F are as follows:

$$A = \frac{k^2(1-x_i^2)(1-xl_i^2)}{(\delta x)^2}, \quad B = \frac{k^2(1-x_{i-1}^2)(1-xl_i^2)}{(\delta x)^2} \tag{32}$$

$$C = \frac{1}{(f_2(xl_i) - f_1(xl_i))^2(\delta y)^2} = D, \quad E = G(x_i, yl_j)\frac{k^2(1-x_i^2)(1-xl_i^2)}{4\delta x\delta y} \tag{33}$$

$$F = G(x_{i-1}, yl_j)\frac{k^2(1-x_{i-1}^2)(1-xl_i^2)}{4\delta x\delta y} \tag{34}$$

We note here, that an advantage of using MAC cell, is that the pressure boundary condition is not needed at the boundaries where the velocity vector is specified, since the domain boundaries are chosen to fall on velocity nodes. For the cells adjacent to the upper wall $(y=1)$, we get from the v-momentum equation

$$p_{ij+1}^n = p_{ij}^n + \{f_2(xl_i) - f_1(xl_i)\}\delta y\, \mathrm{Vcd}_{ij}^n \tag{35}$$

Therefore, the Poisson equation for pressure, for the cells adjacent to the upper wall $(y=1)$, is

$$\begin{aligned}&(A+B+D+E-F)p_{ij}^n + (E-A)p_{i+1j}^n - (B+F)p_{i-1j}^n + (F-E-D)p_{ij-1}^n \\ &\quad + Fp_{i-1j-1}^n + [f_2(xl_i) - f_1(xl_i)]\delta y(E-F)\,\mathrm{Vcd}_{ij}^n - Ep_{i+1j-1}^n \\ &\quad + [f_2(xl_{i+1}) - f_1(xl_{i+1})]\delta y E\,\mathrm{Vcd}_{i+1j}^n - [f_2(xl_{i-1}) - f_1(xl_{i-1})]\delta y F\,\mathrm{Vcd}_{i-1j}^n \\ &= -\left[\frac{\mathrm{Div}_{ij}^n}{\delta t} + k(1-xl_i^2)\frac{\mathrm{Ucd}_{ij}^n - \mathrm{Ucd}_{i-1j}^n}{\delta x} - \frac{\mathrm{Vcd}_{ij-1}^n}{\delta y(f_2(xl_i) - f_1(xl_i))}\right]\end{aligned} \tag{36}$$

DOI: 10.1002/fld

where p_{ij}^n is the pressure located at the cell centre inside the flow domain. The Poisson equation for pressure for the cells adjacent to the inlet boundary at $x=-1$ may be expressed as

$$(A+C+D)p_{ij}^n - Ap_{i+1j}^n - Dp_{ij-1}^n - Cp_{ij+1}^n$$
$$= -\left[\frac{\mathrm{Div}_{ij}^n}{\delta t} + k(1-xl_i^2)\frac{\mathrm{Ucd}_{ij}^n}{\delta x} + \frac{\mathrm{Vcd}_{ij}^n - \mathrm{Vcd}_{ij-1}^n}{\delta y}\right] \tag{37}$$

Similarly, the Poisson equations for pressure for the cells adjacent to the lower wall ($y=0$) and outlet boundary ($x=1$) are obtained. The Poisson equation for pressure has been solved iteratively by the successive over-relaxation (SOR) method. The value of the over-relaxation parameter depends on the chosen number of grid points. The choice 1.5 is found convenient for the grid size used here.

4.4. Pressure and velocity corrections

For computation involving a large number of grid points, a very large number of iteration steps would be needed for satisfactory level of convergence (here the tolerance used for convergence of the SOR iterative scheme is 0.5×10^{-5}). To reduce the computation time for each cycle, the number of iterations in the SOR iteration scheme is kept limited (say, about 20 iterations). However, convergence of the solution for the pressure equation cannot be expected with such a small number of iterations. Therefore, the velocity field obtained after solving the momentum equations using an already known inaccurate pressure field may not satisfy the continuity equation. This necessitates a corrector stage. In this stage pressure and subsequently velocity field are corrected, in the sense that they would satisfy the continuity equation more accurately.

This second stage starts with computing the divergence of velocity field for each cell. If it is found greater than a specified tolerance at any cell in absolute sense, pressure is corrected for each cell in the flow field. The velocity components at the sides of the cell are then adjusted.

The details of the derivation of pressure and velocity correction formulae are omitted here. The final form of the pressure correction formula is

$$p_{ij}^n = p_{ij}^* + \omega_2 \delta p_{ij} \tag{38}$$

where p_{ij}^* is obtained after solving the Poisson equation, $\omega_2(\leqslant 0.5)$ is an under-relaxation parameter and

$$\delta p_{ij} = -\frac{\mathrm{Div}_{ij}^*}{\delta t(A+B+C+D)} \tag{39}$$

where Div_{ij}^* is the value of the divergence of velocity field at the cell (i, j) obtained after solving the Poisson equation for pressure. The velocity correction formulae are

$$u_{ij}^{n+1} = u_{ij}^* + \frac{k(1-x_i^2)\delta t\,\delta p_{ij}}{\delta x} \tag{40}$$

$$u_{i-1j}^{n+1} = u_{i-1j}^* - \frac{k(1-x_{i-1}^2)\delta t\,\delta p_{ij}}{\delta x} \tag{41}$$

$$v_{ij}^{n+1} = v_{ij}^* + \frac{\delta t\,\delta p_{ij}}{(f_2(xl_i) - f_1(xl_i))\delta y} \tag{42}$$

DOI: 10.1002/fld

$$v_{ij-1}^{n+1} = v_{ij-1}^{*} - \frac{\delta t \delta p_{ij}}{(f_2(xl_i) - f_1(xl_i))\delta y} \tag{43}$$

where $u_{ij}^{*}, u_{i-1j}^{*}, v_{ij}^{*}, v_{ij-1}^{*}$ represent the updated velocity field obtained after solving the Poisson equation for pressure.

We note here that the process is iterative since when one cell is adjusted its neighbours are affected. The iteration is carried out by sweeping the mesh columns from left to right starting with bottom row and working upwards.

4.5. Stability restriction

To make the finite-difference scheme numerically stable, certain restrictions are imposed on the mesh sizes δx, δy and also on δt. The time step is governed by two restrictions. The first restriction is related to the convection of the fluid, requiring that the fluid cannot move through more than one cell in one time step. Therefore, the time step must satisfy the inequality

$$\delta t \leqslant \mathrm{Min}\left[\frac{\delta x}{|u|}, \frac{\delta y}{|v|}\right]_{ij} \tag{44}$$

where the minimum is in global sense. Secondly, momentum must not diffuse more than one cell in one time step. This condition, which is related to the viscous effects, according to Hirt's stability analysis implies

$$\delta t \leqslant \mathrm{Min}\left[\frac{Re}{2}\frac{\delta x^2 \delta y^2}{(\delta x^2 + \delta y^2)}\right]_{ij} \tag{45}$$

Denoting the right-hand side of Equation (44) by δt_1 and the right-hand side of Equation (45) by δt_2, we find that both the inequalities are satisfied by taking the time step δt as

$$\delta t = \alpha \mathrm{Min}(\delta t_1, \delta t_2) \tag{46}$$

Here $\alpha(<1)$ is a relaxation factor that lies in the interval $[0.2, 0.4]$.

4.6. Numerical algorithm

One complete calculation cycle comprises the following steps:

Stage 1:

(a) Velocities u_{ij}^{n} and v_{ij}^{n} are initialized at each cell (i, j). This is done either from the results of previous cycle or from the prescribed initial conditions.
(b) Time step (δt) is calculated from stability criteria as explained above.
(c) The Poisson equation for pressure is solved to get the intermediate pressure field (p_{ij}^{*}) using the velocities u_{ij}^{n} and v_{ij}^{n} of the nth time step.

DOI: 10.1002/fld

(d) The momentum equations are solved to get intermediate velocities u_{ij}^* and v_{ij}^* in an explicit manner using the velocities u_{ij}^n, v_{ij}^n and pressure (p_{ij}^*) as found from the solution of the Poisson equation for pressure.

Stage 2:

(e) The maximum cell divergence of velocity field is calculated and is checked with the prescribed tolerance. If satisfied, steady-state convergence or limiting non-dimensional time criteria is checked for whether to stop the calculation. If the maximum divergence is not satisfactorily low, it becomes necessary to go to step (f).

(f) The pressure at each cell of the flow domain is corrected and subsequently the velocities of that and left and bottom neighbouring cells are adjusted to get u_{ij}^{n+1}, v_{ij}^{n+1} and p_{ij}^n. Then step (e) is again performed.

This completes the necessary calculations for advancing the flow field through one cycle in time. The process is to be repeated until steady-state convergence or limiting non-dimensional time is achieved.

4.7. Implementation of the numerical algorithm

For implementation of the finite-difference scheme for obtaining numerical solution, a grid independence study is made in two stages. First, at $Re=600$, u-velocity values at different ordinates in a straight channel are compared with the exact solution as shown in Table I.

Table I shows comparison of exact values of u-velocity with that of the computational values corresponding to different grid sizes for a long straight channel. Next, results for a locally expanded channel for different grid sizes are computed and shown in Table II, which shows that u and v velocities are in good agreement in different grid sizes. It indicates that the results for the grid size 100×50 are reasonably good, at low Reynolds numbers. However, the actual computations have been carried out on a 200×100 uniform grid and all the computations at Reynolds numbers

Table I. Results of different grid sizes for a long straight channel at $Re=600$.

Grid	Property	$Y\to 0$	0.1	0.3	0.5	0.7	0.9	1
100×50	u	0	0.08994	0.20987	0.24985	0.20988	0.08995	0
200×100	u	0	0.08997	0.20989	0.24987	0.20994	0.08998	0
Exact solution	$u=Y-Y^2$	0	0.09000	0.21000	0.25000	0.21000	0.09000	0

Table II. Results of different grid sizes for a locally expanded channel at $Re=2000$ with $X_0=8, M=5, h=1$ at $X=0$.

Grid	Property	$Y\to -1.0$	-0.43	0.20	0.83	1.46	1.76	2.0
100×50	u	0	0.03163	0.11380	0.10851	0.02856	0.01238	0
200×100	u	0	0.03168	0.11387	0.10858	0.02857	0.01232	0
100×50	v	0	-0.00312	-0.00195	0.00401	0.00307	0.00101	0
200×100	v	0	-0.00316	-0.00198	0.00403	0.00302	0.00107	0

DOI: 10.1002/fld

$Re \geqslant 3000$ have been performed using 400×200 grid points. This is so because at higher Reynolds numbers, 200×100 grid is not capable of capturing all the flow-field features.

5. RESULTS AND DISCUSSION

In order to get an idea of grid error in the computed solutions, we computed solution for flow in a typical channel with expansion, given by Equation (9) with parameter values $X_0 = 8$, $h = -1$, for 400×200 and 200×100 grid points, at Reynolds number $Re = 550$, under no external magnetic field.

Figure 4 shows a comparison of the stress distribution on the upper and lower walls of the channel taking mesh spacings $\delta x = \delta y = 0.005$ and 0.01, respectively. The agreement is very good. This supports the view that the computations with 200×100 grid points ought to be quite satisfactory.

The corresponding streamlines are shown in Figure 5. The flow is asymmetric and separates from both the walls. A small eddy is seen attached to the lower wall. From these comparisons, we expect that the computed results with 200×100 uniform grid ought to be quite satisfactory at relatively low Reynolds numbers.

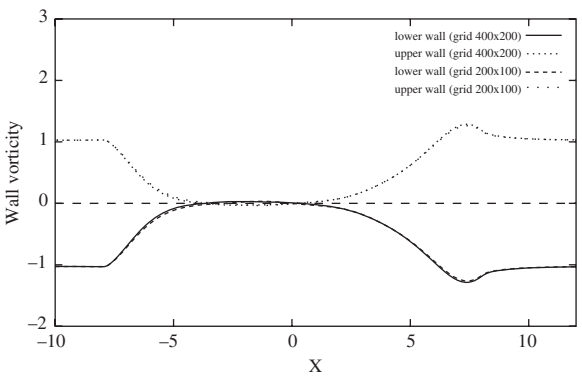

Figure 4. Wall shear stress distribution at $Re = 550$, $M = 0$ for 400×200 and 200×100 grid points.

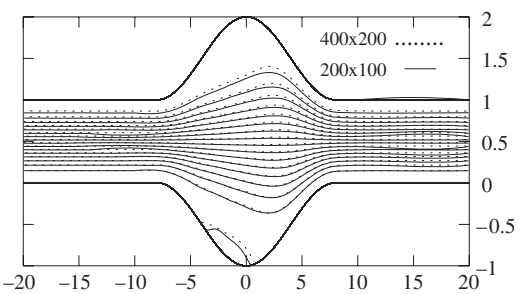

Figure 5. Comparison of streamlines at $Re = 550$, $M = 0$ for (a) 400×200 grid points and (b) 200×100 grid points.

DOI: 10.1002/fld

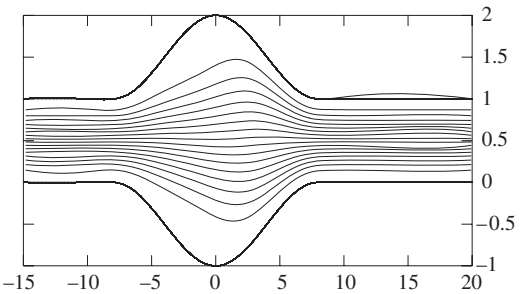

Figure 6. Streamlines for $Re = 550, M = 1.5$.

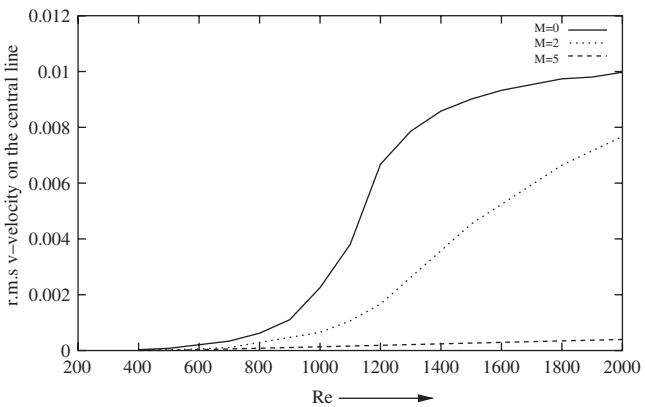

Figure 7. Distribution of r.m.s v-velocity on the central line of the channel corresponding to Hartmann numbers $M = 0,\ 2$ and 5.

The effect of a transverse magnetic field corresponding to Hartmann number $M = 1.5$ on this flow is shown in Figure 6. We see that, as a result of the applied transverse magnetic field, the flow has turned symmetric and that the small eddy at the lower wall in Figure 5 has disappeared. Similar behaviour has been observed at higher Reynolds numbers, which is discussed in the following.

For the above symmetric channel expansion, computed solution in the absence of applied external transverse magnetic field ($M = 0$) shows symmetric unseparated flow for Reynolds numbers in the range $Re \leqslant 500$. Separated asymmetric flows are found to occur in the Reynolds number range $500 < Re < 1100$, the flow separating from both the walls of the channel. For $Re \geqslant 1100$, the flow is asymmetric and separates only from the upper wall, there being no separation from the lower wall, that is, the flow attaches to the lower wall. An eddy is formed in the expansion region of the upper wall, its size growing larger with increasing Reynolds number. This is in conformity with corresponding results for the case of symmetric channels with sudden expansions studied by earlier authors referred to in Section 1.

As a measure of asymmetry, we have calculated the root-mean-square (r.m.s) v-velocity on the central line of the channel for values of Hartmann numbers $M = 0, 2$ and 5 at different Reynolds numbers presented in Figure 7.

DOI: 10.1002/fld

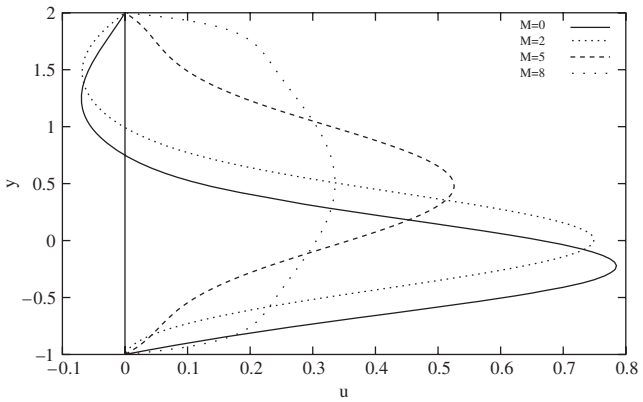

Figure 8. Velocity profiles for different values of Hartmann number M at $X=0$ for $Re=2000$.

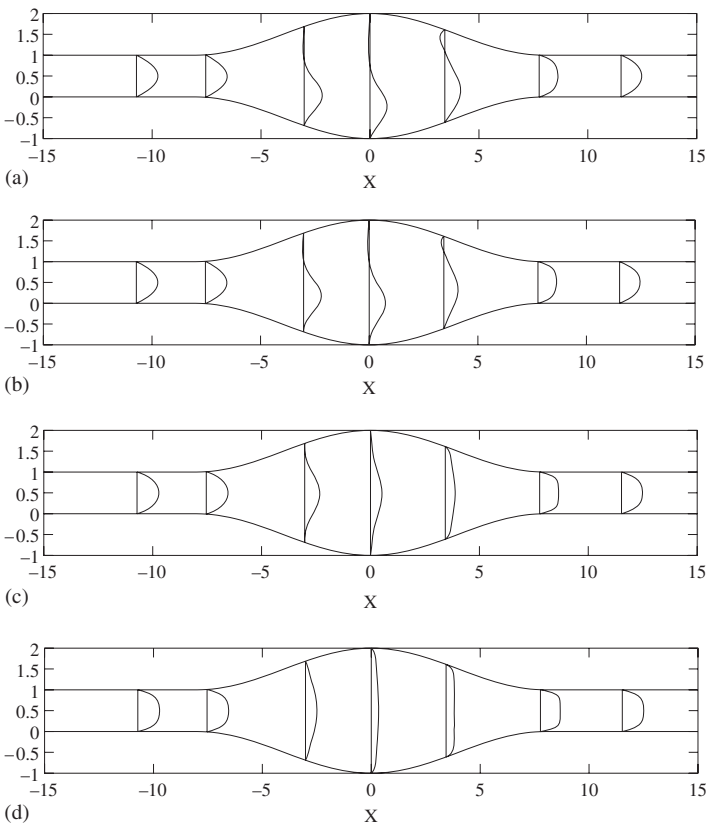

Figure 9. u-Velocity profiles for different Hartmann numbers at $Re=2000$: (a) $M=0$; (b) $M=2$; (c) $M=5$; and (d) $M=8$.

DOI: 10.1002/fld

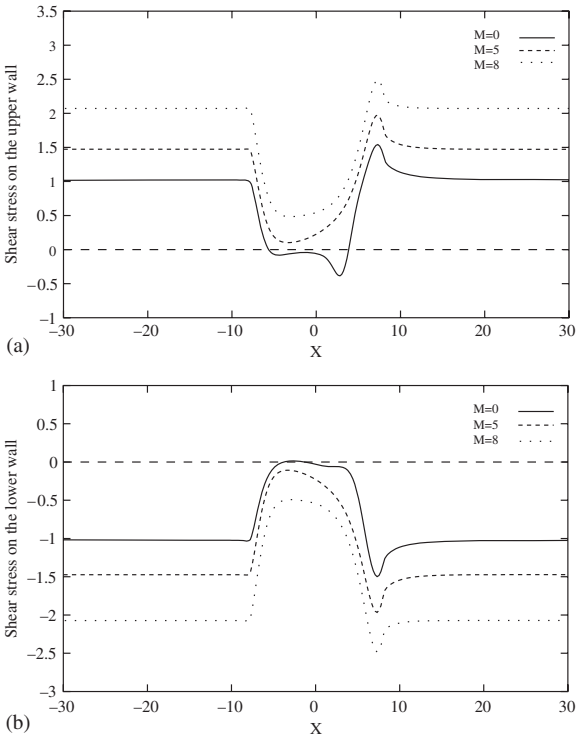

Figure 10. Distribution of shear stress on (a) upper and (b) lower walls for different values of Hartmann number M at $Re = 1250$.

If the flow in the channel be symmetric, the r.m.s. of the v-velocity on the central line of the channel should be zero. From Figure 7, it is clear that for $M = 0$ the flow becomes asymmetric (indicated by a non-zero value of the r.m.s velocity) after a certain Reynolds number. This asymmetry almost disappears when the strength of the magnetic field M is increased to 5, in this case. Comparing the r.m.s v-velocity curves, it may be noted that the flow in the case $M = 2$ is less asymmetric than that in the case $M = 0$.

Figure 8 shows the velocity profiles for different values of M at the station $X = 0$ for $Re = 2000$. It may be seen that for $M = 0$, the flow separates only at the upper wall and the corresponding velocity profile is asymmetric. Moreover, as the Hartmann number M increases, the velocity profiles gradually become symmetric and the separation disappears. It is evident from this figure that the peak value of the u-velocity decreases with increase in the value of the Hartmann number M.

Figures 9(a)–(d) show a series of u-velocity profiles at $Re = 2000$ at different positions of the channel for Hartmann numbers $M = 0, 2, 5$ and 8, respectively. Figure 9(a) shows that for $M = 0$ the flow separates at the upper wall in the expansion region of the channel, but there is no separation at the lower wall. Figure 9(b) shows that for $M = 2$ the flow separates at both the upper and lower walls. In Figure 9(c), it is seen that for $M = 5$, the flow separates at both upper and lower walls. Velocity profiles are now much more symmetric about the centre line ($Y = \frac{1}{2}$) of the channel. For $M = 8$ at $Re = 2000$, since there is no point of inflexion on the u-velocity profiles, as shown in Figure 9(d), we conclude that the flow separation completely disappears. It may also be noted from

DOI: 10.1002/fld

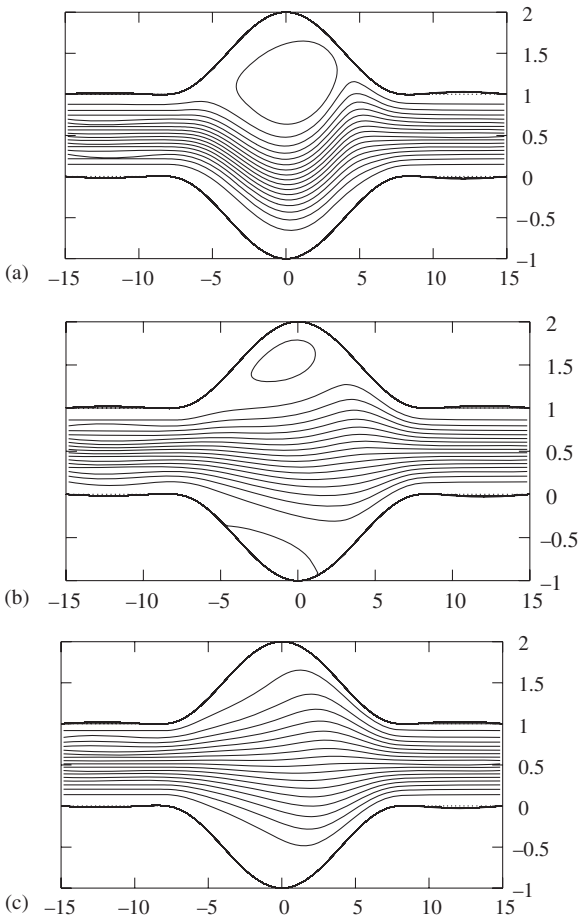

Figure 11. Streamlines at $Re = 1100$ for Hartmann numbers: (a) $M = 0$; (b) $M = 2$; and (c) $M = 3.3$.

Figure 9(d) that the profiles become symmetric. This indicates that the flow becomes symmetric with a sufficient increase in the strength of the magnetic field.

5.1. Wall vorticity

Distribution of shear stress on the upper and lower walls for different values of Hartmann number M at $Re = 1250$ is shown in Figures 10(a) and (b). From Figure 10(a) it appears that as the strength of the magnetic field M increases, the length of the separation zone decreases and ultimately no separation occurs. Similar is the case for the shear stress distribution on the lower wall, shown in Figure 10(b).

5.2. Streamlines and vorticity contours

Streamlines of the flow for different values of the Hartmann number M at Reynolds number $Re = 1100$ are shown in Figures 11(a)–(c). Figure 11(a) shows that for $M = 0$, there is a recirculation

DOI: 10.1002/fld

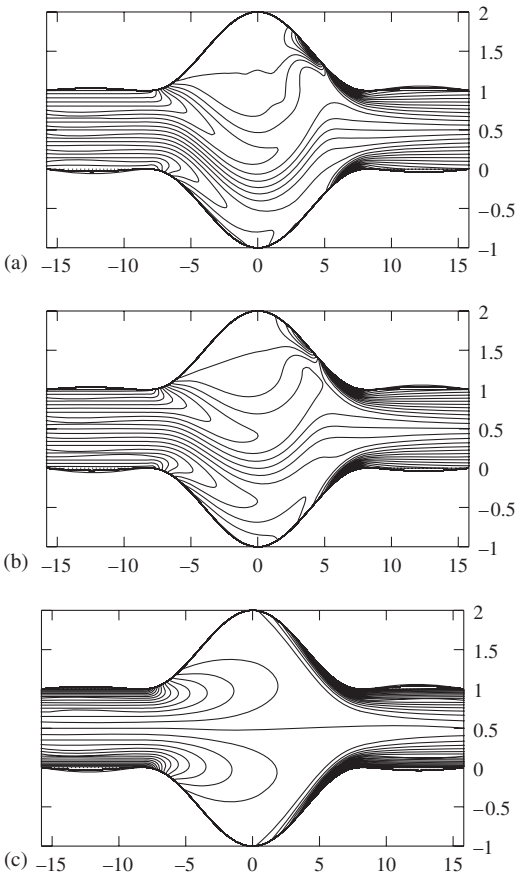

Figure 12. Vorticity contours of the flow at $Re=2000$, for Hartmann numbers: (a) $M=0$; (b) $M=2$; and (c) $M=5$.

zone near the upper wall in the expansion region of the channel, but no corresponding recirculation zone near the lower wall. The flow remains attached to the lower wall. Therefore, inspite of the fact that there is geometric symmetry, the flow is asymmetric at $Re=1100$. Comparing Figures 11(a) and (b) it may be observed that the recirculation zone for $M=2$ is smaller than that for $M=0$. Further, from Figure 11(c) it is clearly seen that the flow becomes symmetric at $M=3.3$ and the recirculation zone completely disappears.

Figures 12(a)–(c) show the vorticity contours of the flow for different values of the Hartmann number M at $Re=2000$. These vorticity contours show that there is flow asymmetry for $M=0$ and 2, while for $M=5$ the vorticity contours are symmetric, so that the flow also turns symmetric about the channel central line.

The streamlines for flow in the channel at Reynolds number $Re=3000$ and Hartmann number $M=0$ are shown in Figures 13(a)–(c) at three different non-dimensional times $t=1000.45$, $t=1207.96$, and at $t=1415.48$, respectively. Eddies formed in the upper-wall expansion region indicate large areas of recirculating zone. It may be observed that the recirculating zone slowly

DOI: 10.1002/fld

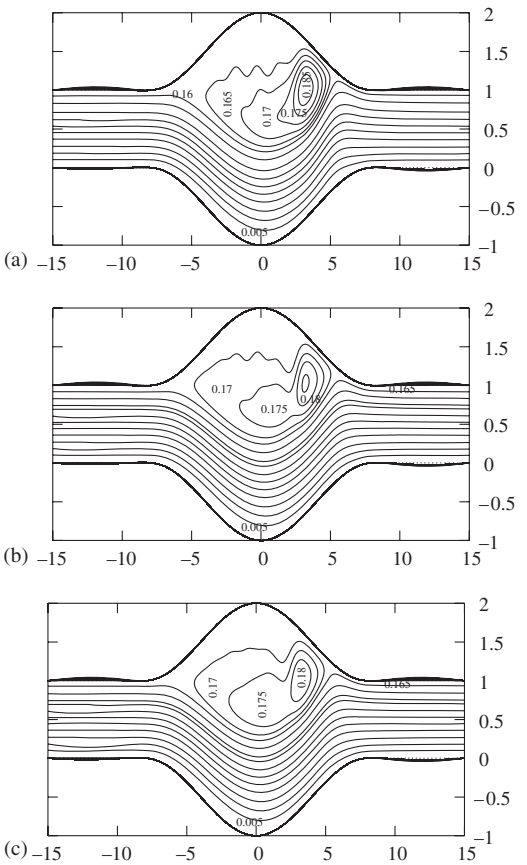

Figure 13. Streamlines for Hartmann number $M=0$ and $Re=3000$ at different non-dimensional times: (a) $t=1000.45$; (b) $t=1207.96$; and (c) $t=1415.48$.

reduces in size for increasing non-dimensional time. The flow is asymmetric with respect to the central line $Y=\frac{1}{2}$ of the channel and is slightly unsteady. However, after sufficiently large time the flow is found to turn steady, for example, for non-dimensional time $t\geqslant 1415$.

Here, a flow is considered steady if it satisfies the condition over all the mesh points

$$\max_{i,j}\left[\left|\frac{\partial u}{\partial t}\right|,\left|\frac{\partial v}{\partial t}\right|\right]\leqslant\varepsilon \tag{47}$$

where ε is a prescribed small positive quantity. In our computations, we have taken $\varepsilon=0.5\times 10^{-5}$.

The streamlines at Reynolds number $Re=3000$ and Hartmann number $M=5$ are shown in Figures 14(a)–(c) at non-dimensional times $t=603.13$, $t=810.65$, and $t=1018.2$, respectively. No recirculating zone may be seen near the upper wall. Small eddies formed near the lower wall in the expansion region may be seen in these figures showing the flow to be asymmetric.

Thus, the flow becomes steady and symmetric as the intensity of the applied magnetic field increases. Strength of the magnetic field needed to arrest separation depends on the aspect ratio

DOI: 10.1002/fld

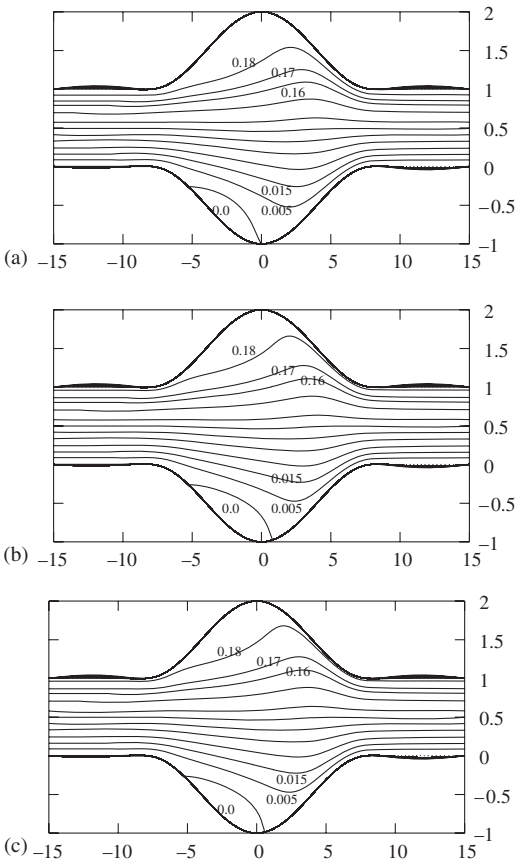

Figure 14. Streamlines for Hartmann number $M=5$ and $Re=3000$ at non-dimensional times: (a) $t=603.13$; (b) $t=810.65$; and (c) $t=1018.2$.

(the ratio of the amplitude of the wall expansion to the semi-wavelength of it) and on the Reynolds number.

5.3. Pressure: central line, upper and lower walls

The pressure distributions along the upper wall, central line and lower wall of the channel at $Re=3000$ for different Hartmann numbers $M=0,\ 5$, and 10 are shown in Figures 15(a)–(c).

In Figure 15(a), we see that for Hartmann number $M=0$, as the flow approaches the expansion region of the channel, the upper wall pressure slightly deceases and attains a minimum value in the downstream region. The upper wall pressure rapidly decreases and attains a minimum value in the downstream region for Hartmann number $M=5$. The upper wall pressure deceases more rapidly and attains a minimum value in the downstream region for Hartmann number $M=10$. It is interesting to see that as the Hartmann number increases, the upper wall pressure decreases rapidly and attains minimum values in the downstream regions. Similar is the case for the pressure distributions on the central line and lower wall, as shown in Figures 15(b) and (c).

DOI: 10.1002/fld

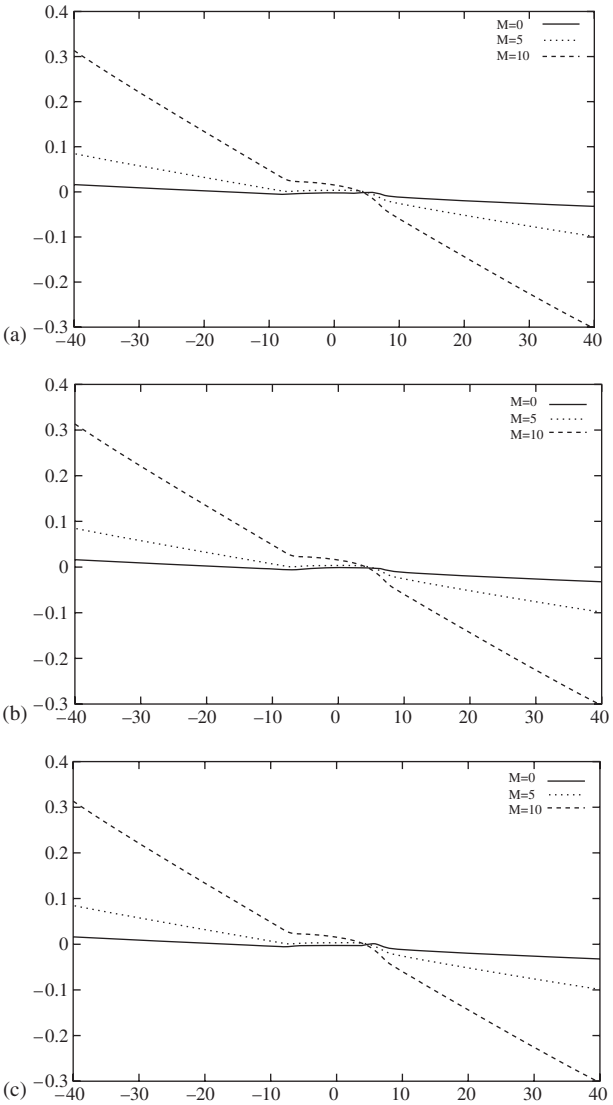

Figure 15. Pressure distribution for Hartmann numbers $M = 0, 5, 10$ at $Re = 3000$: (a) upper wall; (b) central line; and (c) lower wall.

6. FLOW AT HIGHER REYNOLDS NUMBERS

In the present work, we assume the flow to be laminar. Transition experiments conducted by Patel and Head [26] show that the plane Poiseuille flow undergoes transition to turbulence for Reynolds number as low as 1000, the Reynolds number being formed using the channel centreline velocity and half the channel width. It may be noted that according to Equation (10) the centreline velocity in our work is $U/4$,(not U) and h^* is the channel width used to define the Reynolds

DOI: 10.1002/fld

number as $Re = Uh^*/\nu$. Thus, the experimental value of the transition Reynolds number, in our notation, would be 8000 ($= 1000 \times 4 \times 2$). Keeping this in mind, our computations are at relatively low Reynolds numbers. As the Reynolds number increases, the flow takes a long time to reach a steady state, if at all it reaches a steady state. The two-dimensional flow shows signs of instability. Determination of the precise Reynolds number needs further investigation. Owing to this we have not computed solution for higher Reynolds numbers.

7. CONCLUSION

The flow of a viscous incompressible electrically conducting fluid through a long channel with local symmetric expansion has been investigated for several small values of the Hartmann number. For increasing Reynolds number, the flow becomes asymmetric and separates from both the walls for a certain value of the Reynolds number in the absence of a transverse magnetic field. With further increase in Reynolds number, the flow separates from one of the walls and remains attached to the other wall. A recirculating zone is formed near the wall from which the flow separates, whose size increases with increase in the value of the Reynolds number. However, with increase in the strength of the magnetic field the flow becomes symmetric again and the flow separation disappears. The strength of the magnetic field needed to arrest separation depends on the geometry of the walls and on the Reynolds number. At relatively higher laminar Reynolds numbers, the flow turns slightly unsteady and takes much longer time to reach a steady state. Application of a transverse magnetic field of suitable strength is likely to suppress perturbations and leads to a higher transition Reynolds number. Thus, a transverse magnetic field has a stabilizing effect in controlling flow separation and unsteadiness in the channel, as also in delaying transition to turbulence.

ACKNOWLEDGEMENTS

The authors thank the referee(s) (anonymous) for valuable comments and for pointing out several references that enabled improved presentation of this paper.

REFERENCES

1. Lee JS, Fung YC. Flow in locally constricted tubes at low Reynolds number. *Journal of Applied Mechanics* (ASME) 1970; **37**:9–16.
2. Lee TS. Steady laminar fluid flow through variable constrictions in vascular tube. *Journal of Fluids Engineering* (ASME) 1994; **116**:66–71.
3. Cheng RT. Numerical solution of the Navier–Stokes equations by the finite-element methods. *Physics of Fluids* 1972; **15**:2098–2105.
4. Vradis G, Zalak V, Bentson J. Simultaneous variable solutions of the incompressible Navier–Stokes equations in general curvilinear co-ordinate systems. *Journal of Fluids Engineering* (ASME) 1992; **114**:299–305.
5. Mahapatra TR, Layek GC, Maiti MK. Unsteady laminar separated flow through constricted channel. *International Journal of Non-linear Mechanics* 2002; **37**:171–186.
6. Durst F, Pereira JCF, Tropea C. The plane symmetric sudden-expansion flow at low Reynolds numbers. *Journal of Fluid Mechanics* 1993; **248**:567–581.
7. Durst F, Melling A, Whitelaw JH. Low Reynolds number flow over a plane symmetrical sudden expansion. *Journal of Fluid Mechanics* 1974; **64**:111–128.
8. Cherdron W, Durst F, Whitelaw JH. Asymmetric flows and instabilities in symmetric ducts with sudden expansion. *Journal of Fluid Mechanics* 1978; **84**:13–31.

DOI: 10.1002/fld

9. Fearn RM, Mullin T, Cliffe KA. Nonlinear flow phenomena in a symmetric sudden expansion. *Journal of Fluid Mechanics* 1990; **211**:595–608.
10. Restivo A, Whitelaw JH. Turbulence characteristics of the flow downstream of a symmetric plane sudden expansion. *Journal of Fluids Engineering* (ASME) 1978; **100**:308.
11. Sobey IJ, Drazin PG. Bifurcations of two-dimensional channel flows. *Journal of Fluid Mechanics* 1986; **171**: 263–287.
12. Pramanik S, Layek GC, Mahapatra TR, Majumdar HP. Numerical study of viscous flow through a locally expanded channel. *International Journal of Applied Mechanics and Engineering* 2004; **9**(3):557–571.
13. Schlichting H. *Boundary Layer Theory* (6th edn), Translated by J. Kestin. McGraw-Hill: New York, 1968.
14. Gad-el-Hak M, Bushnell DM. Separation control: review. *Journal of Fluids Engineering* (ASME) 1991; **113**:5–30.
15. Midya C, Layek GC, Gupta AS, Mahapatra TR. Magnetohydrodynamic viscous flow separation in a channel with constrictions. *Journal of Fluids Engineering* (ASME) 2003; **125**:952–962.
16. Reddy SC, Schmid PJ, Bagget P, Henningson DS. On stability of streamwise streaks and transition thresholds in plane channel flows. *Journal of Fluid Mechanics* 1998; **365**:269–303.
17. Krasnov DS, Zienicke E, Zikanov O, Boeck T, Thess A. Numerical study of instability of the Hartmann layer. *Journal of Fluid Mechanics* 2004; **504**:183–211.
18. Moresco P, Alboussiere T. Experimental study of the instability of the Hartmann layer. *Journal of Fluid Mechanics* 2004; **504**:167–181.
19. Harlow FH, Welch JE. Numerical calculation of time dependent viscous incompressible flow of fluid with free surface. *Physics of Fluids* 1965; **8**:2182–2189.
20. Niyogi P, Chakrabartty SK, Laha MK. *Introduction to Computational Fluid Dynamics*. Pearson Education: Delhi, 2005; 436–451.
21. Shercliff JA. *A Textbook of Magnetohydrodynamics*. Pergamon Press: New York, 1965.
22. Sutton GW, Sherman A. *Engineering Magnetohydrodynamics*. McGraw-Hill: New York, 1965.
23. Patankar SV. *Numerical Heat Transfer and Fluid Flow*. McGraw-Hill: New York, 1980.
24. Roache PJ. *Computational Fluid Dynamics* (revised english edn). Hermosa Publishers: New Mexico, 1985.
25. Maikap TK, Mahapatra TR, Layek GC, Niyogi P, Ghosh AK. Unsteady laminar separated flow through channel with double constriction. *Computational Fluid Dynamics Journal* 2003; **12**:53–64.
26. Patel VC, Head R. Some observations on skin friction and velocity profiles in fully developed pipe and channel flows. *Journal of Fluid Mechanics* 1969; **38**:181–201.

DOI: 10.1002/fld